Optics Communications 368 (2016) 134–140

Contents lists available at ScienceDirect

Optics Communications

journal homepage: www.elsevier.com/locate/optcom

Three-dimensional ghost imaging using acoustic transducer

Chi Zhang [a], Shuxu Guo [a], Jian Guan [a], Junsheng Cao [b], Fengli Gao [a,*]

[a] State Key Laboratory on Integrated Optoelectronics, College of Electronic Science and Engineering, Jilin University, Changchun 130012, China
[b] Changchun Institute of Optics, Fine Mechanics and Physics, Chinese Academy of Sciences, Changchun 130033, China

ARTICLE INFO

Article history:
Received 20 December 2015
Received in revised form
24 January 2016
Accepted 26 January 2016
Available online 12 February 2016

Keywords:
Coherence imaging
Photoacoustics
Image formation theory

ABSTRACT

We propose a novel three-dimensional (3D) ghost imaging method using unfocused ultrasonic transducer, where the transducer is used as the bucket detector to collect the total photoacoustic signal intensity from spherical surfaces with different radius circling the transducer. This collected signal is a time sequence corresponding to the optic absorption information on the spherical surfaces, and the values at the same moments in all the sequences are used as the bucket signals to restore the corresponding spherical images, which are assembled as the object 3D reconstruction. Numerical experiments show this method can effectively accomplish the 3D reconstruction and by adding up each sequence on time domain as a bucket signal it can also realize two dimensional (2D) ghost imaging. The influence of the measurement times on the 3D and 2D reconstruction is analyzed with Peak Signal to Noise Ratio (PSNR) as the yardstick, and the transducer as a bucket detector is also discussed.

1. Introduction

Ghost imaging, as a newly emerging optical imaging method, has arouse broad concern because of its advantages on imaging in complex environment, separation between detection and imaging and so on. The incipient experiment of ghost imaging was conducted with entangled photons [1–3]. The original ghost imaging realized with pseudo-thermal light emerged many achievements [4–12]. In the recent several years, with the successive achievements on lensless ghost imaging [13], true thermal light ghost imaging [14,15] and advanced algorithm to enhance the PSNR [16–21], ghost imaging ceases from being just a hypothetical theory, and many of the researches are turning into a series of practical applications [22–31]. For example, in researches on optical encryption [22,28], ghost imaging was applied in 3-D optical encryption that a larger key space can be generated, on biomedical imaging [29], and on remote sensing, the 3-D ghost imaging ladar has been manufactured which can image objects from over 1 km and obtain 60 cm axis solution. By taking the structural properties of the recovered images into account, the reconstruction quality can be further improved [31]. However, achievements on 3D ghost imaging within a short distance are rarely reported.

As a burgeoning imaging method, photoacoustic imaging possesses both the advantages of the thermal imaging's high solution and ultrasonic imaging's nondestructive examination and strong penetrating power, which endows it with broad application prospect [32–36]. Photoacoustic imaging is based on the photoacoustic effect, which is aroused by the sound wave emitted by the object when irradiated by laser pulse and absorbing photons. The photoacoustic signal is acquired by an ultrasonic transducer, and processed by a reconstruction algorithm, it can provide the object's optic absorption characteristics [33]. Considering the similarity which both signals detected by the unfocused transducer and the bucket detector are corresponding to the optic absorption characteristics of the objects, a possibility appears that the photoacoustic imaging method can be applied to ghost imaging.

We propose a novel 3D ghost imaging scheme, in which the bucket detector is replaced by an unfocused ultrasonic transducer. Here, the total light intensity obtained by the bucket detector is replaced by the photoacoustic signal, and with a proper modification on traditional ghost imaging algorithm, the object's image can be reconstructed. Since the ultrasonic signal acquired by the unfocused transducer is a time sequence of the spatial sound pressure changing rate against time, the reconstruction result is a 3D deconstruction of the original target. In comparison to the traditional 2D ghost imaging, in our scheme when the laser pulse illuminated on the object reaches a certain intensity, a photoacoustic sequence signal can be obtained by the transducer on the object arm. Meanwhile, the light distribution is recorded on the reference arm records. As long as the object's axial depth on light path direction is no more than the light field's axial correlation depth [37], the object's 3D image can be restored by assembling the transducer-centered spherical surfaces reconstructed by the

* Corresponding author.
E-mail address: gaofl@jlu.edu.cn (F. Gao).

http://dx.doi.org/10.1016/j.optcom.2016.01.078
0030-4018/

3D ghost imaging algorithm.

2. Method

The traditional ghost imaging is consisted of an object arm and a reference arm. As shown in Fig. 1(a), the pseudo-thermal source is acquired by a laser passing through a rotating ground glass and generating a constantly changing speckle pattern, which is separated into two identical beams by a splitter. On the object arm, beam 'a' is projected on the object, modulated by its transmission coefficient $T(x, y, z)$, and acquired by a bucket detector with no spatial solution, where it is recorded as bucket signal B_n. On the reference arm, the speckle pattern on beam 'b' is directly acquired by a spatial-distinguishable CCD, and recorded as $I_n(x, y)$. z_1 represents the distance between pseudo-thermal source and the object, and z_2 represents the distance between pseudo-thermal source and the reference CCD plane. When $z_1 = z_2$ or $|z_1 - z_2|$ is less than the light field axial depth [37], the correlation operation Eq. (1) as below can reconstruct the object's image $\boldsymbol{T}_{GI}$ using the B_n and $I_n(x, y)$ from N measurements.

$$T_{GI}(x, y) = 1/N \cdot \sum_{n=1}^{N} \left(B_n - \langle B_n \rangle\right) I_n(x, y) \tag{1}$$

where the total light intensity is $B_n = \iint I_n(x, y) T(x, y) dxdy$, and its average value is $\langle B_n \rangle = 1/N \cdot \sum_{n=1}^{N} B_n$. As shown in Fig. 1(b), the modification is on the object arm, replacing the bucket detector with an unfocused ultrasonic transducer and z_1 represents the distance between pseudo-thermal source and the central surface of the object. The object and transducer are both placed in viscous transparent media such as water or oil in which the ultrasonic wave declines slower during transmission. The laser path on the object arm is defined as axis 'z'. A photoacoustic signal is stimulated when a laser pulse is projected on the object with the spatial light absorbing coefficient matrix $T(x, y, z)$, and collected as a time sequence by an unfocused transducer on the right end of axis 'z', the nth measurement of which is recorded as $P_n(t)$. Finally, by using the $P_n(t)$ and $I_n(x, y)$ of N measurements in our 3DGI method, a reconstruction of the object can be acquired as $T_{3DGI}(x, y, z)$.

The principle of unfocused ultrasound transducer is shown in Fig. 2. The transducer's wavefront is a spherical surface, so the time sequence $P(t)$ as in the square at time t_1, t_2, t_3 are the total photoacoustic signal intensity of all the sources on the surfaces centered at the detecting point with radius of $R_1 = v_s t_1$, $R_2 = v_s t_2$, $R_3 = v_s t_3$. Since the acoustic pressure signal acquired by the transducer at each moment is a representation of the total optical absorption characteristics on the corresponding spherical surface, so functionally the transducer can be considered equivalent to the bucket detector.

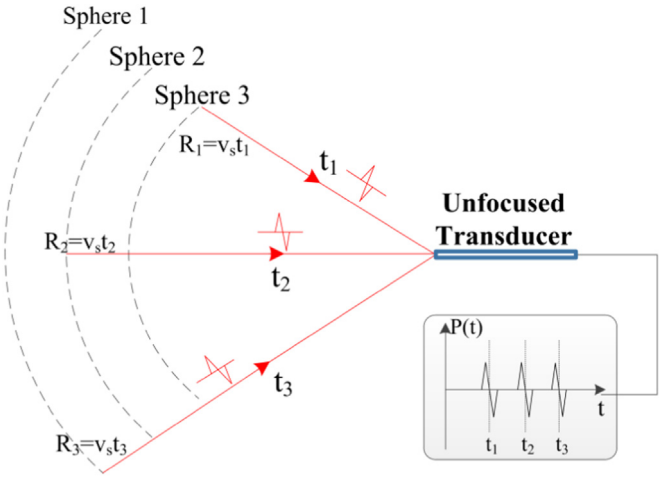

Fig. 2. Schematic diagram of unfocused ultrasonic transducer . V_s: sound velocity.

If the laser pulse lasts shorter than the acoustic confinement time, the acoustic pressure $p(\vec{r}, t)$ at moment t and transducer location $\vec{r}$ in viscous media can be shown as below [32]

$$p(\vec{r}, t) = (\beta/4\pi C_P)\frac{\partial}{\partial t}\int d\vec{r'}\,\frac{1}{\left|\vec{r} - \vec{r'}\right|} \cdot H\left(\vec{r'}, t - \frac{\left|\vec{r} - \vec{r'}\right|}{v_s}\right) \tag{2}$$

where β represents the thermal coefficient of volume expansion, C_P represents specific heat capacities at constant pressure, H represents the heating function and $\vec{r}'$ represents the sound source location. H can be disassemble as below

$$H(\vec{r'}, t') = A_e(\vec{r'}) H_t(t') \tag{3}$$

where A_e is the specific or volumetric optical absorption, and is the laser distribution in time domain. The light field projected on the object is a speckle pattern and pulsing, so Eq. (3) can be modified as below

$$H(\vec{r'}, t') = A_e(\vec{r'}) \delta(t') I(\vec{r'}) \tag{4}$$

where $I(\vec{r}')$ is the light intensity at location $\vec{r}'$ of the speckle pattern on the object. Combining Eq. (4) with Eq. (2), the following equation is established

$$p(\vec{r}, t) = \beta/4\pi C_P \cdot \frac{\partial}{\partial t}\int d\vec{r'}\,\frac{A_e(\vec{r'}) I(\vec{r'})}{\left|\vec{r} - \vec{r'}\right|}\delta\left(t - \frac{\left|\vec{r} - \vec{r'}\right|}{v_s}\right) \tag{5}$$

Integrating the $p(\vec{r}, t)$ in the nth measurement, $p_n(\vec{r}, t)$, in time domain, we can obtain the following equation with proper

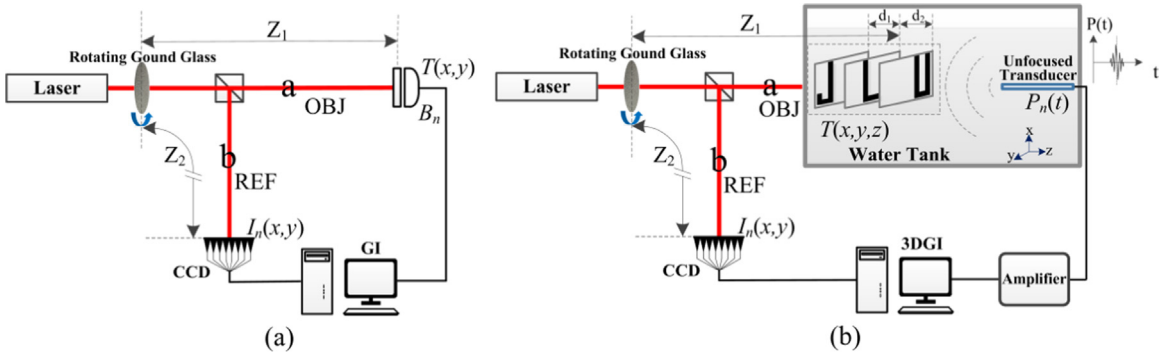

Fig. 1. Schematics of GI and 3DGI systems. (a) Traditional 2DGI method. (b) 3DGI method. OBJ: Object Arm; REF: Reference Arm. z_1: the distance between pseudo-thermal source and the object plane. z_2: the distance between pseudo-thermal source and the reference CCD plane.

transformation

$$S_n(t) = \int_{|\vec{r}-\vec{r}'|=v_s t} A_e(\vec{r}')I_{O,n}(\vec{r}')d\vec{r}' = \frac{4\pi C_P v_s t}{\beta}\int p_n(\vec{r}, t)dt\Big|_t \quad (6)$$

where $I_n(\vec{r}')$ represents the speckle pattern on the spherical surface in the *nth* measurement with radius of $|\vec{r} - \vec{r}'| = v_s t$ centered by the transducer probe. Comparing Eq. (6) with Eq. (1), we can observe a similarity between $S_n(t)$ and the total light intensity B_n in Eq. (1). The difference is that B_n is integration on a flat surface, and $S_n(t)$ is integration on the spherical surface with radius of $|\vec{r} - \vec{r}'|$, so the spherical image can be reconstructed as

$$T(\vec{r}')|_{|\vec{r}-\vec{r}'|=v_s t} = \frac{1}{N}\sum_{n=1}^{N}\left[S_n(t) - \langle S_n(t)\rangle\right]I_n(\vec{r}') \quad (7)$$

where $\langle S_n(t)\rangle = 1/N\cdot\sum_{n=1}^{N} S_n(t)$, so theoretically the reconstruction result $T(\vec{r}')$ of Eq. (7) is an expression of the A_e on the spherical surface.

However, in actual experiments the CCD can only obtain the light distribution on a flat surface, so in the reconstruction process, $I_n(\vec{r}')$ can only be approximated by the detected value $I_n(x, y, z_2)$ where z_2 is a constant as shown in Fig. 1. In Fig. 1(b), the z axial depth of the object is d_1, d_2. When d_1, d_2 meet the GI axial depth conditions [37], we can use the speckle pattern on $z_2 = z_1$ to approximate all the speckle patterns on all the spherical surfaces in the object, so the projection $T(x, y)$ of Eq. (7) on X–y plane can be expressed as below

$$T(x, y) = \frac{1}{N}\sum_{n=1}^{N}\left[S_n(t) - \langle S_n(t)\rangle\right]I_n(x, y, z_2) \quad (8)$$

Using Eq. (8) we can approximately reconstruct the A_e on the spherical surface with radius of $v_s t$. The speckle field $I_n(x, y, z_2)$ in Eq. (8) does not contain the information of axis z, neither does the reconstruction result $T(x, y)$, so the z axial depth of each pixel in $T(x, y)$ is remain to be discussed.

The z axial depth acquisition method above is shown in Fig. 3, where the origin point of the spatial coordinate is the transducer location S. Since the actual spatial locations of all the pixels in $T(x, y)$ are on a spherical surface with the radius of $v_s t$, for any coordinate (x, y) in $T(x, y)$, its **z** axial location can be solve by the distance $l(x, y)$ between the pixel and the projection point of S on X–y plane as below

$$z = -\sqrt{(v_s t)^2 - l^2(x, y)} \quad (9)$$

Combining Eqs. (8) and (9), the 3DGI reconstruction result can be eventually expressed as below

$$T_{3DGI}(x, y, z) = \frac{1}{N}\sum_{n=1}^{N}\left[S_n\left(\frac{\sqrt{z^2 + l^2(x, y)}}{v_s}\right) - \left\langle S_n\left(\frac{\sqrt{z^2 + l^2(x, y)}}{v_s}\right)\right\rangle_n\right] I_n(x, y, z_2) \quad (10)$$

According to Eq. (10), the A_e of the object can be acquired and the 3DGI process is realized.

3. Numerical experiment and discussion

The 3DGI method is carried out by numerical experiment for Fig. 1. The pseudo-thermal light source with $\lambda = 635$nm wave length is numerically generated by a laser beam projected through a rotating ground glass and the transverse size D of the laser beam on the ground glass is $D=1$ mm. Then the beam is divided into two identical beams by a beam splitter prism, one of which is projected on the object in a water tank and the other is directly captured by a CCD with distance $z_2=204.5$ mm to the pseudo-thermal light source (ground glass surface). An unfocused transducer is set on axis z to acquire the photoacoustic signal. The resolution of the adjacent spherical detection surfaces is related to the central frequency of the applied transducer, which decides the imaging resolution of the z axis. The object model in the numerical experiment is three letters 'JLU' on three different flat surfaces on axis z, assuming all letters made of highly opaque material and vertical to axis ***z***. Note that the laser pulse lasts shorter than the acoustic confinement time.

The detailed size of the object is shown in Fig. 4. The size of each surface is 20 mm × 45 mm, the distance from surface 'J' to surface 'L' is d_1 and from surface 'L' to surface 'U' is d_2, where $d_1=d_2=4.5$ mm. The distance from pseudo-thermal light source to surface 'L' is set $z_1 = 204.5mm$ and from the transducer probe location to surface 'U' is 40 mm. It is assumed that each surface's center, the unfocused transducer probe and the laser beam transverse section center are all on the same straight line parallel to axis z. Since the distance from the object to the pseudo-thermal light source is between 200 mm and 209 mm, all the parameters above fulfill the GI axial depth conditions, that is to say, the difference between the object arm and reference arm is under the two-arm light field axial correlation depth, as below [37]

$$|z_1 z_2/(z_1 - z_2)| > D^2/\lambda \quad (11)$$

The simulated photoacoustic signal of the model detected by the transducer is shown in Fig. 5. Obviously, it can be observed that there are four distinct acoustic signal groups in the time sequence simulated by regions of the three letters. This phenomenon is

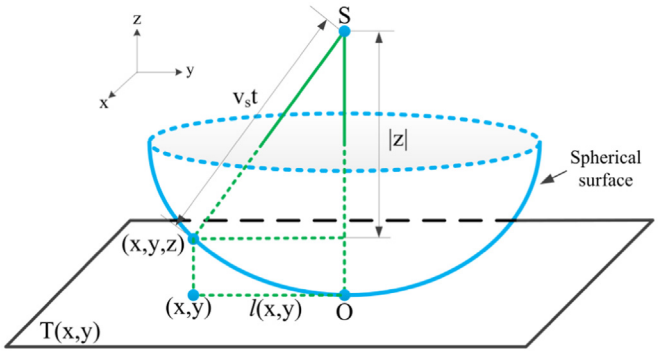

Fig. 3. The sketch of z axial depth acquisition. S: the location of the transducer. $l(x, y)$: the distance between the pixel and the projection point of S on x–y plane.

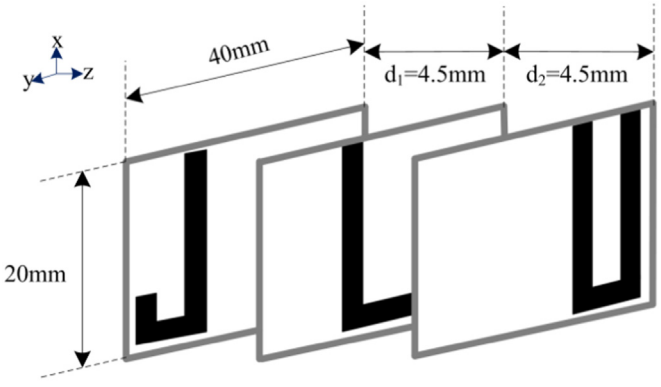

Fig. 4. Detailed dimensional information of the object.

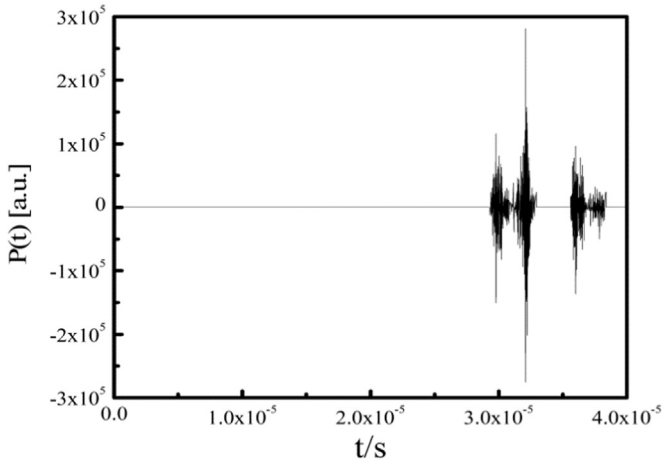

Fig. 5. The photoacoustic signal from the object.

caused by the transducer detecting more than one letter simultaneously.

According to Eq. (7), the signal acquired by the transducer is substantially the changing ratio of the sound pressure signal against time t, so $P_n(t)$ in Fig. 5 has both positive and negative values. But in the 3DGI method we need the actual sound pressure signal as in Eq. (6), which is acquired by an indefinite integration of $P_n(t)$ with an initial value. Here, the initial value is set 0 to compute the sound pressure time sequence $S_n(t)$. In reality $S_n(t)$ is a positive pressure signal, so in the experiment a value is added to modify $S_n(t)$ to insure that there is no negative value and the minimum value is 0. The 3DGI reconstruction result is shown in Fig. 6, where the measurement time is 2000, Fig. 6(a) is the original 3D spatial image of the three letters, Fig. 6(b) is the 3D reconstruction of the object, Fig. 6(c) is the reconstructed images on the sections 40 mm, 44.5 mm, 49 mm to S respectively along the dot lines in Fig. 6(b).

From Fig. 6(b), we can see the reconstruction is a spherical shell centered at location S, since the reconstruction result is the optical absorption information on a series of spherical surfaces. From Fig. 6(c), we can see three clear reconstructed images on the surfaces 'J', 'L' and 'U', which indicates the three light absorbing sections are reconstructed and our 3DGI method is effective. It can also be observed from Fig. 6(c) that letter 'L' is of more clarity than the other two letters, which is because the speckle pattern adopted in all the reconstruction of spherical surfaces is the one on surface 'L' acquired from the reference arm, and the smaller the speckle pattern error is, the more clearer the reconstruction is [15]. Additionally, because of the approximation of the flat speckle pattern to the spherical speckle pattern in the reconstruction process, and the discretization error caused by retrieving the spherical surface from the projection (Fig. 6(c)), there exists a luminance nonuniformity phenomenon on the three sections.

In our method, the 2D GI can also be accomplished when the summation of $S_n(t)$ on the time domain is used as the bucket detecting signal, and the 2D reconstruction can be expressed as below

$$G(x, y) = \frac{1}{N}\sum_{n=1}^{N}\left[\sum_{t} S_n(t) - \langle \sum_{t} S_n(t)\rangle_n\right] I_n(x, y, z_2) \tag{12}$$

The 2D reconstruction results are shown in Fig. 7, where Fig. 7 (a), (b) and (c) are the results with 1000, 2000, 4000 measurements respectively. From Fig. 7 we can see that, with 1000 measurements, the image is almost entirely drenched in noise, while the reconstruction is relatively improved when the measurement time increases to 2000 and with 4000 measurements, the three letters 'JLU' can be clearly distinguished, so the 2D GI is realized with our method and increasing the measurement times can effectively improve the reconstruction quality, which conforms to the traditional 2D GI pattern. Additionally, we can also observe the phenomenon that letter 'L' is slightly clearer than the other two letters, which is still caused by adopting the speckle pattern on surface 'L' in the reconstruction.

In order to demonstrate the influence of measurement times to our 3DGI method, the 3DGI reconstruction results with different measurement times are shown in Fig. 8, where Fig. 8(a), (b) and (c) are the results with 1000, 2000 and 4000 measurements separately. We can see that the reconstruction with 2000 measurements is slightly superior to the 1000 measurements reconstruction, but the 4000 measurements reconstruction is not distinctly improved compared to the 2000 measurements reconstruction, and this phenomenon indicates that the influence of the measurement time on our 3DGI method is a lot more feeble than that on the 2D GI.

Why there exists a distinct difference above between the influence of measurement time to the 3DGI and 2D GI? We further investigate and explain the influence of the measurement time on our 3DGI and 2D GI methods, we use PSNR to quantify the reconstruction quality. The reconstruction PSNR of the 3DGI and 2D GI are shown in Fig. 9, where the red, black and blue curves are corresponding to the PSNR on sections 'L', 'J' and 'U' in 3DGI separately, and the green curve is the PSNR of the 2D GI results. In Fig. 9, the PSNR of image 'L' is obviously higher than image 'J' and image 'U' , which is coherence to the visual effects in Fig. 6(c) and Fig. 7, and this attributes to using the speckle field on section 'L' in the reconstruction. Additionally, the PSNR of image 'J' is higher than image 'U', although their z axial deviations are identically d, and this is mainly attributed to the higher sparsity of surface 'J' than surface 'U'. Moreover, the PSNR of all the three surfaces are all higher than that of the 2D GI result, which is because in the 3DGI

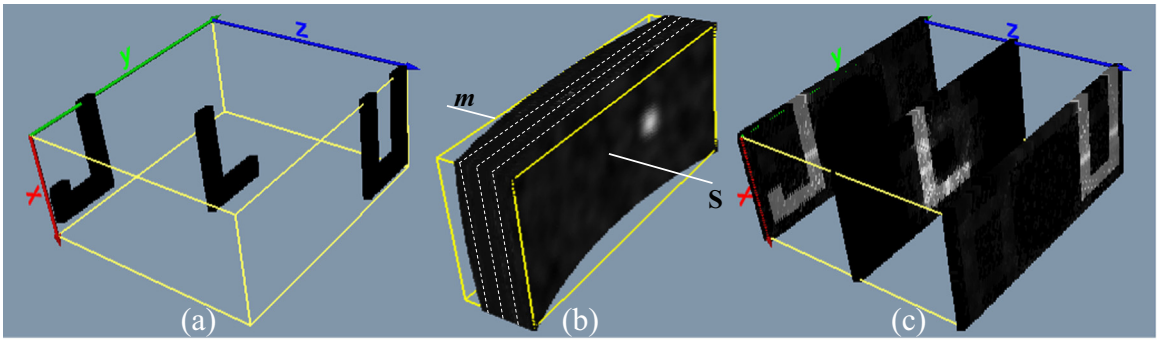

Fig. 6. The reconstruction result of 3DGI. (a) The original 3D spatial image of the three letters. (b) The 3D reconstruction of the object. (c) The reconstructed images on the three sections. m: z axis line; S:transducer location.

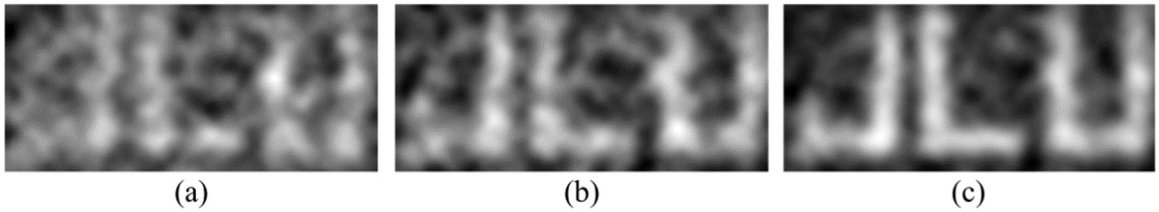

Fig. 7. The 2D GI reconstruction results. (a) The result with 1000 measurements; PSNR: 7.873 dB. (b) The result with 2000 measurements; PSNR: 8.9444 dB. (c) The result with 4000 measurements; PSNR: 9.3443 dB.

method the original image $A_e(\vec{r}')|_{|\vec{r}-\vec{r}'|=v_s t_i}$ on all the spherical surface are more highly sparse than the 2D projection of the object on X–y plane. Besides, due to the high sparsity above, under 1000 measurements the PSNRs of 'J', 'L' and 'U' grow rapidly with the measurement time increasing, and over 1000 measurements the three PSNRs grow very slowly, which quantitatively matches Fig. 8. Meanwhile, the PSNR of 2D GI keeps increasing with the measurement time growing, which is coherence to Fig. 7 visually.

One condition needs to be fulfilled when the transducer can function as the bucket detector. The object has to be fully covered by the detectable region of the transducer, which is to say the acoustic signals from all over the target are collected, so the object needs to completely locate in the farfield of the transducer. Meanwhile, for an ideal needle-like unfocused transducer (a point detector) the acoustic beam main-lobe of the transducer is a sphere, same shape as the detection surface, which means the acoustic signal degradation during transferring from different sources on a spherical detection surface to the transducer is coherent. However, in practice there are no ideal point detectors, and the radiated sound pressure of the transducer can be expressed as below [38]

$$p_r = j\omega\frac{\rho u_0 a^2}{2r_s}\left[\frac{2J_1(ka\sin\theta)}{ka\sin\theta}\right]e^{j(\omega t-kr_s)} \tag{13}$$

where ω is the ultrasonic angular frequency, ρ is the medium density, u_0 is the peak amplitude of transducer velocity, k is wavenumber, a is the transducer radius, θ is the angle between the line from the detected point to the transducer center and axis z, and r_s is distance from the acoustic source to the probe center. The simulated sound pressure distribution radiated by a cylindrical unfocused transducer (central frequency: 2 MHz, radius: 0.5 mm) is shown in Fig. 10, where Fig. 10 (a) is the sectional sound pressure distribution along axis z (the sound axis), Fig. 10 (b) is the isoamplitude surface sketch and Fig. 10 (c–e) are the sound pressure distribution on section 'J', 'L' and 'U'. The acoustic intensity is normalized and shown by the color map and gray map, the white dash lines represent the spatial position of our object ('J', 'L' and 'U') in the acoustic field, the three colored dash lines represent three isoamplitude surfaces and the black solid arc represents the

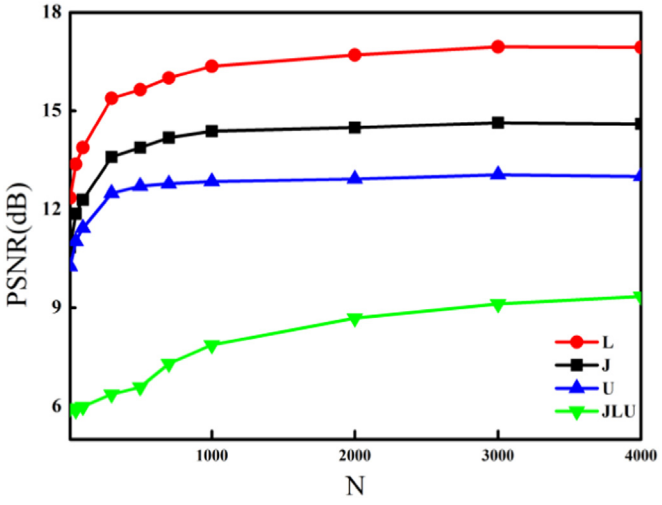

Fig. 9. The PSNR curves of our 3DGI and 2D GI with different measurement times. (For interpretation of the references to color in this figure legend, the reader is referred to the web version of this article.)

detection surface.

From Fig. 10 (a) and (c–e) we can see that the object is still completely located in the farfield of the transducer, which means the acoustic signal from every source point on the object is collected. Meanwhile from Fig. 10 (a) and (b) we also can observe that the main-lobe is not a strict sphere but ellipsoid-like, which causes the acoustic signal degradation during transferring from different sources on a spherical detection surface to the transducer is not coherent. So in practice after the reconstruction using Eq. (10), the reconstruction value of each point should to be amended by Eq. (13) according to the applied transducer.

4. Conclusion

We propose a novel 3D ghost imaging using unfocused ultrasonic transducer as the bucket detector, which makes a bucket

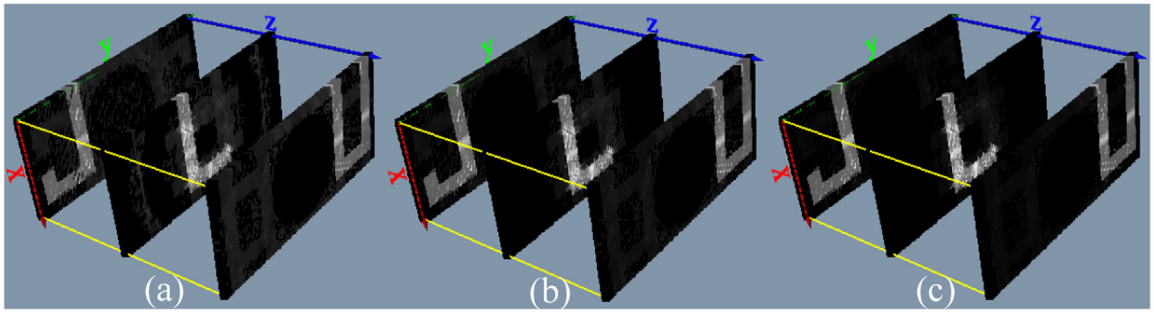

Fig. 8. The reconstruction result of 3DGI with different measurement times. (a) The result with 1000 measurements; PSNR:14.2767 dB(J); 16.3668 dB(L); 12.9688 dB(U). (b) The result with 2000 measurements; PSNR:14.4188 dB(J); 16.6912 dB(L); 13.1227 dB(U). (c) The result with 4000 measurements; PSNR:14.4373 dB(J); 16.9183 dB(L); 13.1261 dB(U).

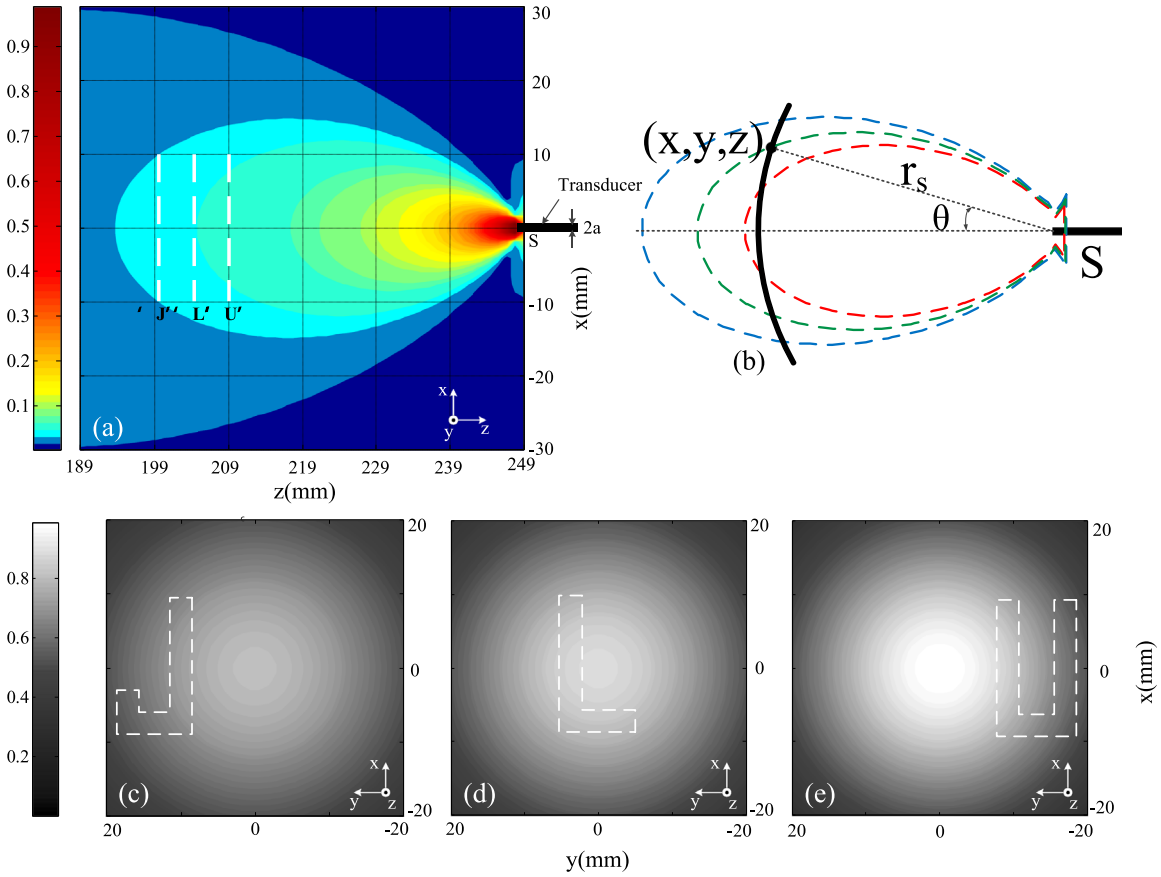

Fig. 10. The spatial sound pressure distribution of a cylindrical unfocused transducer. (a) The sound pressure distribution on axis *z*; (b) Isoamplitude surfaces sketch; (c) Sound pressure distribution on section 'J';(d) Section 'L';(e) Section 'U';

signal be a time sequence correlated to the 3D spatial information. When axial depth of the object along the light path meets the traditional ghost imaging conditions, by using the speckle pattern on a section in the object to carry out correlation operation with the serialized bucket signal, our 3DGI can be realized. Additionally, if the summation of a time sequence is used as a bucket signal, the 2D GI can be also realized. In this paper, we also investigate the influence of the measurement time to our method and make discussions on the transducer as a bucket detector. To our knowledge, this is the first thought that photoacoustic imaging is brought into ghost imaging to accomplish 3D ghost imaging, and we believe that our 3DGI method provides a novel thought and a practical solution.

Acknowledgments

The authors are grateful to the Young Scientists Fund of the National Natural Science Foundation of China (Grant no. 61204055), the Natural Science Foundation (Grant no. 20140101175JC and no. 20160101284JC) and the Young Science and research Fund (Grant no. 20130522188JH) of Science and Technology Development Program of Jilin Province, China, for the support in the work.

References

[1] T.B. Pittman, Y.H. Shih, D.V. Strekalov, A.V. Sergienko, Optical imaging by means of two-photon quantum entanglement, Phys. Rev. A 52 (1995) 3429–3432.
[2] D.V. Strekalov, A.V. Sergienko, D.N. Klyshko, Y.H. Shih, Observation of two-photon "ghost" interference and diffraction, Phys. Rev. Lett. 74 (18) (1995) 3600–3603.
[3] R.E. Meyers, K.S. Deacon, Quantum Ghost Imaging Experiments at ARL, in: Quantum Communications And Quantum Imaging Viii, 2010, p. 7815.
[4] R.S. Bennink, S.J. Bentley, R.W. Boyd, "Two-photon" coincidence imaging with a classical source, Phys. Rev. Lett. 89 (2002) 113601.
[5] A. Gatti, E. Brambilla, M. Bache, L.A. Lugiato, Correlated imaging, quantum and classical, Phys. Rev. A 70 (2004) 013802.
[6] A. Gatti, E. Brambilla, M. Bache, L.A. Lugiato, Ghost imaging with thermal light: comparing entanglement and classical correlation, Phys. Rev. Lett. 93 (2004) 093602.
[7] A. Valencia, G. Scarcelli, M. D'Angelo, Y. Shih, Two-photon imaging with thermal light, Phys. Rev. Lett. 94 (2005) 063601.
[8] Y.J. Cai, S.Y. Zhu, Ghost imaging with incoherent and partially coherent light radiation, Phys. Rev. E 71 (2005) 056607.
[9] D.Z. Cao, J. Xiong, K. Wang, Geometrical optics in correlated imaging systems, Phys. Rev. A 71 (2005) 13801.
[10] A. Gatti, M. Bache, D. Magatti, E. Brambilla, F. Ferri, L.A. Lugiato, Coherent imaging with pseudo-thermal incoherent light, J. Mod. Optics 53 (2006) 739–760.
[11] M. Bache, D. Magatti, F. Ferri, A. Gatti, E. Brambilla, L.A. Lugiato, Coherent imaging of a pure phase object with classical incoherent light, Phys. Rev. A 73 (2006) 053802.
[12] J.H. Shapiro, Computational ghost imaging, Phys. Rev. A 78 (2008) 061802.
[13] G. Scarcelli, V. Berardi, Y. Shih, Phase-conjugate mirror via two-photon thermal light imaging, Appl. Phys. Lett. 88 (2006) 061106.
[14] Y.H. Zhai, X.H. Chen, D. Zhang, L.A. Wu, Two-photon interference with true thermal light, Phys. Rev. A 72 (2005) 043805.
[15] X.H. Chen, Q. Liu, K.H. Luo, L.A. Wu, Lensless ghost imaging with true thermal light, Opt. Lett. 34 (2009) 695–697.
[16] O. Katz, Y. Bromberg, Y. Silberberg, Compressive ghost imaging, Appl. Phys. Lett. 95 (2009) 131110.
[17] W.L. Gong, S.S. Han, A method to improve the visibility of ghost images obtained by thermal light, Phys. Lett. A 374 (2010) 1005–1008.
[18] F. Ferri, D. Magatti, L.A. Lugiato, A. Gatti, Differential Ghost Imaging, Phys. Rev. Lett. 104 (2010) 253603.
[19] B.Q. Sun, S.S. Welsh, M.P. Edgar, J.H. Shapiro, M.J. Padgett, Normalized ghost imaging, Opt. Express 20 (2012) 16892–16901.
[20] W. Chen, X.D. Chen, Marked ghost imaging, Appl. Phys. Lett. 104 (2014) 251109.
[21] C. Zhang, S.X. Guo, J.S. Cao, J. Guan, F.L. Gao, Object reconstitution using

pseudo-inverse for ghost imaging, Opt. Express 22 (2014) 30063–30073.
[22] P. Clemente, V. Duran, V. Torres-Company, E. Tajahuerce, J. Lancis, Optical encryption based on computational ghost imaging, Opt. Lett. 35 (2010) 2391–2393.
[23] G.R. Ying, Q.W. Shen, S.S. Han, A two-step phase-retrieval method in Fourier-transform ghost imaging, Opt. Commun. 281 (2008) 5130–5132.
[24] P.L. Zhang, W.L. Gong, X. Shen, S.S. Han, Correlated imaging through atmospheric turbulence, Phys. Rev. A 82 (2010) 33817.
[25] S.M. Zhao, H. Yang, Y.Q. Li, F. Cao, Y.B. Sheng, W.W. Cheng, L.Y. Gong, The influence of atmospheric turbulence on holographic ghost imaging using orbital angular momentum entanglement: simulation and experimental studies, Opt. Commun. 294 (2013) 223–228.
[26] C.Q. Zhao, W.L. Gong, M.L. Chen, E.R. Li, H. Wang, W.D. Xu, S.S. Han, Ghost imaging lidar via sparsity constraints, Appl. Phys. Lett. 101 (2012) 141123.
[27] B.I. Erkmen, Computational ghost imaging for remote sensing, J. Opt. Soc. Am. A 29 (2012) 782–789.
[28] W. Chen, X.D. Chen, Ghost imaging for three-dimensional optical security, Appl. Phys. Lett. 103 (2013) 221106.
[29] J. Bertolotti, E.G. van Putten, C. Blum, A. Lagendijk, W.L. Vos, A.P. Mosk, Non-invasive imaging through opaque scattering layers, Nature 491 (2012) 232–234.
[30] M. Bina, D. Magatti, M. Molteni, A. Gatti, L.A. Lugiato, F. Ferri, Backscattering differential ghost imaging in turbid media, Phys. Rev. Lett. 110 (2013) 083901.
[31] H. Yu, E.R. Li, W.L. Gong, S.S. Han, Structured image reconstruction for three-dimensional ghost imaging lidar, Opt. Express 23 (2015) 14541–14551.
[32] M.H. Xu, L.H.V. Wang, Time-domain reconstruction for thermoacoustic tomography in a spherical geometry, IEEE Trans. Med. Imaging 21 (2002) 814–822.
[33] M.H. Xu, L.V. Wang, Universal back-projection algorithm for photoacoustic computed tomography, Pro. Biomed. Opt. Image 5697 (2005) 251–254.
[34] X. Jin, L.V. Wang, Thermoacoustic tomography with correction for acoustic speed variations, Phys. Med. Biol. 51 (2006) 6437–6448.
[35] H.F. Zhang, K. Maslov, G. Stoica, L.H.V. Wang, Functional photoacoustic microscopy for high-resolution and noninvasive in vivo imaging, Nat. Biotechnol. 24 (2006) 848–851.
[36] L.V. Wang, Tutorial on photoacoustic microscopy and computed tomography, IEEE J. Sel. Top. Quant. 14 (2008) 171–179.
[37] W.L. Gong, S.S. Han, The influence of axial correlation depth of light field on lensless ghost imaging, J. Opt. Soc. Am. B 27 (2010) 675–678.
[38] J. Zemanek, Beam behavior within the nearfield of a vibrating piston, J. Acoust. Soc. Am. 49 (1971) 181–191.